On the role of intergranular nanocavities in long-term stress corrosion cracking of Alloy 690

Zhao Shen[1*], Edward Roberts[1], Naganand Saravanan[1], Phani Karamched[1], Takumi Terachi[2], Takuyo Yamada[2], Shengchuan Wu[3], Edmund Tarleton[1], David E.J. Armstrong[1], Philip J. Withers[4], Koji Arioka[2], Sergio Lozano-Perez[1]

[1] Department of Materials, University of Oxford, Parks Road, OX1 3PH, Oxford, UK

[2] Institute of Nuclear Safety Systems, Inc. (INSS), 64 Sata, Mihama-cho, Mikata-gun, Fuki, Mihama, 919-1205, Japan

[3] State Key Laboratory of Traction Power, Southwest Jiaotong University, Chengdu 610031, PR China

[4] Henry Royce Institute, Department of Materials, The University of Manchester, Manchester, M13 9PL, UK

[*]Corresponding author: 952911809@qq.com

Abstract: The life extension of nuclear power plants beyond 60-years relies on the integrity of the steam generator tubes during the extended life. Alloy 690 steam generator tubes have been generally believed to be resistant to stress corrosion cracking (SCC) failures until the recent unexpected observation of intergranular cavities during long-term SCC testing. Here, a multi-technique characterization approach has been used to study the behaviour of 30% cold worked samples exposed to long-term SCC testing at constant load. This has provided quantitative results on the effect of intergranular cavities and oxidation ahead of the crack tip. SCC mechanisms of creep cavity formation and associated oxidation through the cavity networks are discussed and the required stress to failure calculated, providing a quantitative measure of their weakening effect and a reliable way of assessing and predicting this important degradation problem.

Key words: Alloy 690; Stress corrosion cracking; Intergranular nanocavity; Pressurized water reactor; Grain boundary strength.

1. Introduction

Intergranular stress corrosion cracking (IGSCC) of Alloy 600 has been identified in boiling water reactor (BWR) and pressurized water reactor (PWR) nuclear power plants [1-5]. In response to the serious impact of IGSCC in Alloy 600, Alloy 690 was designed to better resist IGSCC by increasing the Cr content to ~30 wt.%. As such, Alloy 690 has replaced Alloy 600 in many manufactured components such as steam generator tubes, control rod drive mechanism nozzles, and pressurizer heater sleeves in PWR [6-11]. To date, no incidence of IGSCC of Alloy 690 has been reported in PWRs in service in either primary or secondary circuits since its first use in the late 1980s. These results suggest that Alloy 690 may be immune to IGSCC under the operating conditions representative of PWRs. Current regulations allow for a 20-year extension to the 40-year operating license of a PWR. It is hoped that a second life extension may be possible, taking the operating lifetime to 80-years. However, to achieve this objective, a better understanding of long-term IGSCC in Alloy 690 is required, despite its excellent corrosion performance to date.

In a recent review on IGSCC of Alloy 690, Moss et al. [9] reported that dynamic straining is required to consistently initiate IGSCC cracks in PWR primary water. In addition, an IGSCC model was proposed by these authors to explain the occurrence of IGSCC under dynamic straining but not under constant deflection or constant load tests. In this model [9], IGSCC crack propagation is proposed to consist of four stages: 1) a protective Cr_2O_3 oxide film is initially formed on the specimen surface over grain boundaries (GBs); 2) successive rupture and repair of the Cr_2O_3 oxide film under dynamic straining depletes the Cr content in the GBs; 3) the Cr-depleted GBs can no longer provide enough Cr to support the formation of a protective oxide film, which exposes the GBs to the high-temperature water; 4) the unprotected GBs are further oxidized, resulting in crack propagation along the weakened interfaces under subsequent dynamic straining. According to this model, the absence of IGSCC in constant deflection and load testing is proposed to be due to stress relaxation and absence of mechanisms to rupture the oxide film, respectively [9].

For Alloy 690 components in nuclear reactors, it is generally believed that they are exposed to a load with limited or no dynamic straining. According to the theory proposed by Moss et al. [9], Alloy 690 should thus be immune to IGSCC crack initiation without dynamic straining. However, recent long-term constant load studies on Alloy 690 with prior cold work (CW) show that these conditions can lead to the occurrence of IGSCC crack growth [6,7]. This suggests that the mechanisms controlling the IGSCC crack initiation and growth are likely to be different. CW is introduced to simulate its service condition since some degree of CW in local regions is inevitable during the manufacturing, welding, transportation, and assembly processes [12,13]. Bruemmer et al. [12] reported that intergranular cavities and cracked carbides are consistently observed in CW (above 20% cold-rolling) Alloy 690 that has a high density of intergranular carbides and that it has a relatively high IGSCC susceptibility. However, the IGSCC susceptibility is remarkably reduced in the CW Alloy 690 after a short recovery anneal is applied that alters local strain and stress without removing the prior CW-induced GB damage (cavities and cracked carbides). Hence, these authors proposed that the accumulation of high GB strain and stress due to prior CW, instead of GB damage, might be responsible for the enhanced susceptibility to IGSCC. A more detailed study on IGSCC of the CW Alloy 690 conducted by the same research group shows that cavities are frequently observed along GBs extending to the specimen surface, suggesting an important role of the intergranular cavities on IGSCC crack growth [7,14]. Further analysis of the region ahead of the IGSCC crack tips by this group revealed that nearly all shallow surface cracks were associated with a high density of intergranular cavities ahead of the open crack [7,14].

Creep on Ni-alloys was studied by Was' group in the 90s [REF to 3 Met Trans A papers that the reviewer suggested]. In these papers creep is suggested to play a relevant role in the deformation under PWR operating temperatures, with steady-state creep rates inversely correlated with carbon and chromium concentrations in solid solution. Intergranular cavitation and fracture were observed in austenitic alloys after constant extension rate tests (CERTs) and constant load tests (CLTs) in an Ar atmosphere. It was postulated that increasing the Cr content would reduce creep rates, although the formation of cavities would ultimately control IG failure by ductile overload due to the reduction in effective area.

While creep damage was accepted as a plausible mechanism of IGSCC of CW Alloy 690 [6], in a recent study conducted by Yonezawa et al. [53], it was argued that the results in [6] were not sufficient to support the creep damage hypothesis. Yonezawa et al. [53] believed that to confirm the creep damage hypothesis as the mechanism of IGSCC of CW Alloy 690, it is necessary to prove that not only is creep a necessary condition but also a sufficient condition. In other words, it is necessary to show not only that the temperature dependency of crack growth rate and creep cavity formation are similar, but also that cavity formation and deformation have the same stress dependencies. However, the stress dependency was neither observed in three-point bent beam IGSCC tests nor in reserve U-bend specimen IGSCC tests [53]. Hence, Yonezawa et al. [53] suggested that the creep damage might be not the mechanism of IGSCC of CW Alloy 690.

Although the formation of intergranular cavities is expected to have a significant effect on IGSCC crack growth under constant load [6,7,14], to date, the observation of intergranular cavities in Alloy 690 has been very limited due to the difficulties in conducting long-term IGSCC crack growth testing and micro-to-nano scale analyses. As a result, the mechanisms controlling long-term IGSCC crack growth at constant load remain unclear and require further study. The high-resolution microscopy techniques have achieved remarkable improvements recently, which have significantly advanced our understanding of a range of previously unresolved issues [15-19]. Here, we use a combination of microscale secondary electron microscopy (SEM), energy dispersive X-ray (EDX), electron back scattered diffraction (EBSD), nanoscale on-axis transmission Kikuchi diffraction (TKD), transmission electron microscopy (TEM), and electron energy loss spectroscopy (EELS) to study Alloy 690 before and after a long-term IGSCC testing at constant load.

2. Experimental

2.1 Materials and long-term IGSCC testing

The Alloy 690 used in this study was taken from an industrial ingot of the type that is used in operating PWR plants. The material was received in a thermally treated (TT) condition, after being solution-treated at 1075 ºC for 0.5 h in air followed by water-cooling, and then heat-treated at 700 ºC for 15 h followed by air-cooling. Its chemical composition is 30.18 Cr, 9.42 Fe, 0.019 C, 0.30 Si, 0.32 Mn, 0.04 Cu, 0.009 P, 0.0006 S, and balance Ni (wt. %). Its grain size is about 100 µm. CW was introduced by 3 passes of uni-directional rolling at room temperature to a total thickness reduction of 30%, which is referred to as 30% CW.

The IGSCC testing was conducted by the Institute of Nuclear Safety Systems (INSS) using a pre-cracked (in air) 0.5T compact tension (CT) specimen in the T-L direction (crack growth direction parallel to the rolling direction and crack plane perpendicular to the plane of the plate) tested in an autoclave at constant load in 360 ºC water with 500 ppm B + 2 ppm Li + 30 cc/kg dissolved H_2. The initial stress intensity factor value (K) for the CT specimen with a shallow fatigue pre-crack is

30 MPa·m$^{1/2}$. The depth of the fatigue pre-crack is about 2 mm and the thickness of the CT specimen is 12.5 mm. The shallow fatigue pre-crack was produced by fatigue using a load ratio (R=K_{min}/K_{max}=0.1) of 8 Hz with the K_{max} below the stress intensity used for the IGSCC testing. The test duration is 26576 h. After the IGSCC testing, the CT specimen was cut into two halves by electrical discharge machining; one half (A) was fractured by fatigue in air for fractographic analysis and the other (B) polished for cross-sectional analysis. It is worth noting that the IGSCC propagation occurred very locally and most of the regions ahead of the fatigue pre-crack were still intact when the test was concluded. In addition, due to the high IGSCC resistance of the Alloy 690, the total length of the local IGSCC crack was less than 600 μm. Hence, the K value is assumed to be constant for the duration of the test.

2.2 Characterization techniques

A cross-section of the CT specimen after IGSCC testing was analysed by SEM using a Zeiss Crossbeam 540 equipped with EDX and EBSD detector systems. The data were subsequently post-processed by Channel 5 software. Inverse pole figure-z axis (IPFZ) and Kernel misorientation (KMO) maps were calculated automatically by the software. A dual beam Zeiss NVision 40 focused ion beam (FIB) was used to prepare TEM samples with a thickness less than 50 nm. On-axis TKD analysis was conducted using a Zeiss Merlin SEM equipped with a EBSD detector with an Optimus TKD head [20]. The data were subsequently post-processed by Channel 5 software to obtain pattern quality, phase, IPFZ, and misorientation (MO) maps. High-angle annular dark field (HAADF) imaging and EELS were conducted with an aberration-corrected JEOL ARM200F equipped with an EELS detector.

2.3 Micro-mechanical testing and finite element modelling

A dual beam Zeiss NVision 40 FIB-SEM was used to prepare site-specific micro-cantilevers. The micro-cantilevers have an equilateral triangular cross-section and a target width and length of 3 and 15 μm. The cantilevers were milled such that the GB plane is near orthogonal to the surface and is located in the first fifth of the beam. Once prepared, the micro-cantilevers were tested in a Keysight G200 series nano-indenter using a diamond Berkovich tip. The indenter tip was placed at the end of the cantilever. The cantilever was deflected by the tip at a constant rate of 5 nm·s^{-1}, during which a load–displacement curve was simultaneously recorded. More details about this micro-mechanical testing technique can be found in [21].

To obtain quantitative information regarding the strength of the GBs in the presence of cavities, carbides, and intergranular oxides, finite element analysis (using Abaqus software) was conducted to model the fracture and plastic deformation of the cantilevers. This formulation was developed as a crystal plasticity user material (UMAT) from the original implementation by Dunne et al. [22]. Details of the plastic strain calculations and parameters used can be found in [23].

A total of 45592 linear elements with 8 Gauss points per element were used to represent the cantilever. A biased mesh was fitted towards the GB and carbides or cavities. A displacement of u = -3 μm was applied near the end of the cantilever to simulate the loading from the nano-indenter tip. The elastic properties of the material were taken from published in literature c_{11}= 258 GPa, c_{12} = 136 GPa, c_{44} = 172 GPa [24]. Twelve $\langle 1\bar{1}0\rangle\{111\}$ FCC slip systems were included with an initial critically resolved shear stress (CRSS) of ${\tau_c}^0 = 675$ MPa. The maximum allowed separation was chosen to be δ^{max} = 20 nm as this matches the experimental fracture well. Carbides were modelled as rigid bodies having the following properties E = 325 GPa, v = 0.336 [25]. Cavities were modelled as an absence of material. Further details regarding the definition of material properties used in the modelling can be found in [26,27]. A cohesive surface was used to incorporate the effect of interfaces (matrix-carbide and matrix-

oxide) [28]. The cantilever simulations provide a direct comparison to the experimental observations and a way of benchmarking multiple scenarios that would be too time consuming to characterize experimentally [23].

3. Results

3.1 Microstructural analysis prior to IGSCC testing

To compare the crystallographic structure of the Alloy 690 before and after the 30% CW, EBSD analysis was conducted. Figs. 1a and b show the grain shape, IPFZ, and KMO images of the Alloy 690 before and after the 30% CW, respectively. It is evident that the CW has introduced significant deformation into the matrix with the GB region apparently preferentially deformed. SEM imaging shows that the GBs in the materials with and without CW have similar morphologies, decorated by semi-continuous carbides (Figs. 1c and d). The average size and the GB coverage of the carbides are about 300 nm and 60%, respectively. It is also clear that several intergranular carbides are cracked (Fig. 1d). Similar results have been reported by Bruemmer et al. [12], and the authors attributed it to the CW-induced damage. Low-energy EDX mapping (5 kV) shows that the intergranular carbides are enriched in C and Cr and depleted in Ni and Fe. It is worth noting that both the carbide and cavity coverages mentioned in this study were measured based on the 2-dimensional (2D) images (percentage of the trace of the GB).

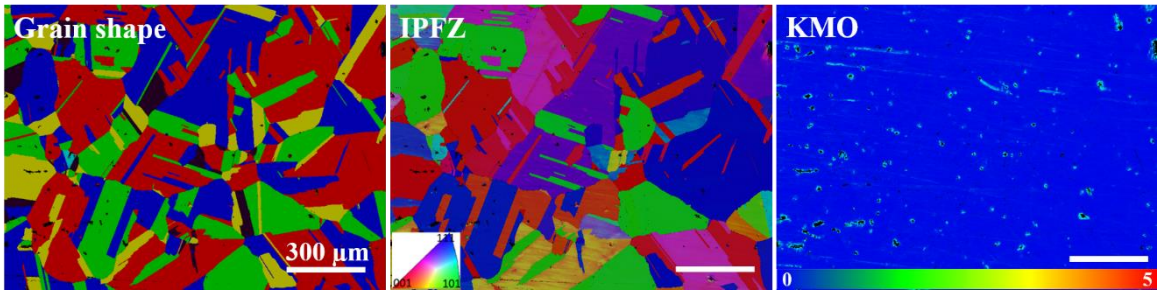

(a)

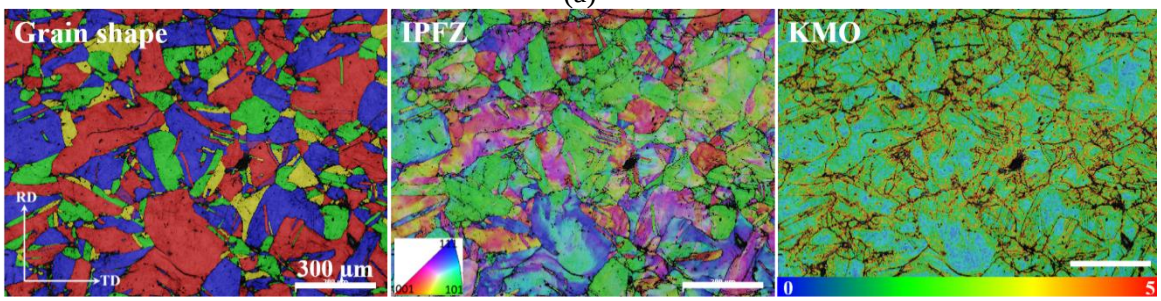

(b)

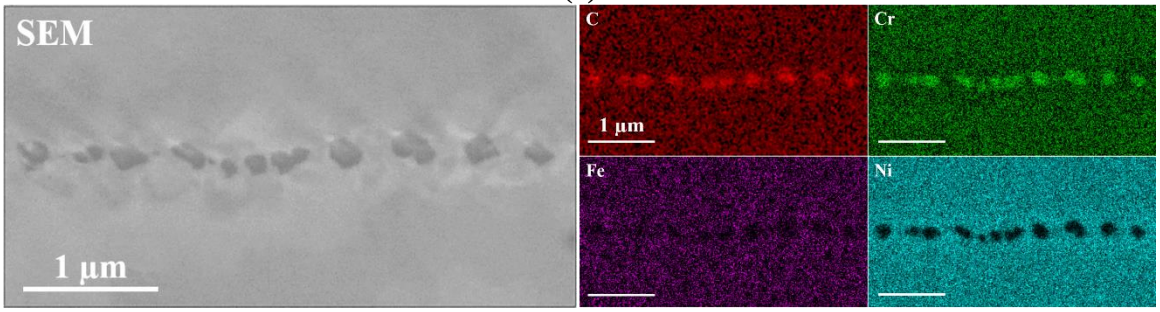

(c)

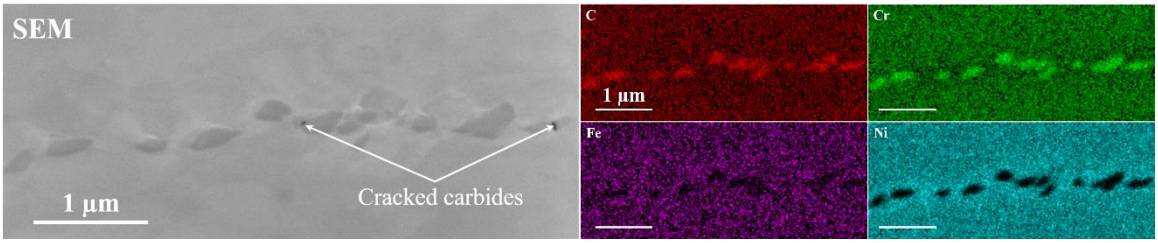

(d)

Fig. 1. Microstructural analysis prior to the IGSCC initiation testing. Grain shape, IPFZ, and KMO maps of Alloy 690 (a) before and (b) after CW. Typical back-scattered SEM morphology and EDX chemical composition around the GBs of Alloy 690 (c) before and (d) after CW.

3.2 Microstructural analysis after IGSCC testing

A detailed examination on the fracture surface (half specimen A) shows that IGSCC has only occurred local to the fatigue pre-crack (see Fig. 2a). The other half of the CT specimen (B) was used to study the crack tip region. A typical region showing the nature of the IGSCC crack is shown in Fig. 2a. Higher magnification of the crack shows the existence of regions with a cavity-like morphology (Fig. 2a). This observation suggests that the intergranular cavities may exist ahead of the IGSCC crack tip. To confirm this observation, TEM foils containing the IGSCC cracks were prepared from half B. A typical result observed by HAADF imaging is shown in Fig. 2b, which validates the hypothesis that a large number of intergranular cavities exist ahead of the IGSCC crack tip. Interestingly, examination of the region within 500 µm from the IGSCC crack shows that cavities also exist at some GBs (Fig. 2b). These GBs were always several matrix grains (more than 2 grains) away from the IGSCC crack. Hence, it is very likely that these GBs were disconnected to the IGSCC crack. Such cavities are not observed beyond 500 µm from the IGSCC crack under SEM examination. 40 high-angle GBs (HAGBs) with intergranular cavities were examined and the morphology of the intergranular cavities can be mainly divided into two types. 38 of them belong to type 1, where the cavities are separated by the semi-continuous carbides, as shown in the Fig. 2c (left). The remaining 2 GBs belong to type 2; these appear to be decorated by continuous carbides. The cavities in these GBs are narrow and interconnected with each other, as shown in Fig. 2c (right). It is worth noting that the GBs with cavities were all identified to be HAGBs and no cavities were observed at low-angle GBs (LAGBs) or coincidence site lattice boundaries (CSLBs). Since most of the GBs in this material belong to type 1, the current study will mainly focus on this type of GB.

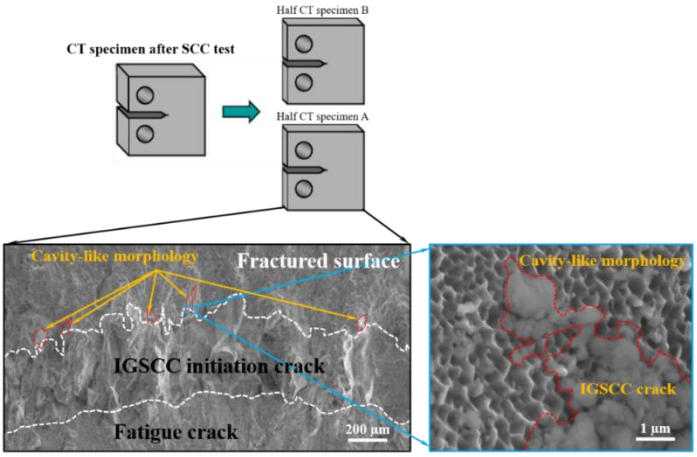

(a)

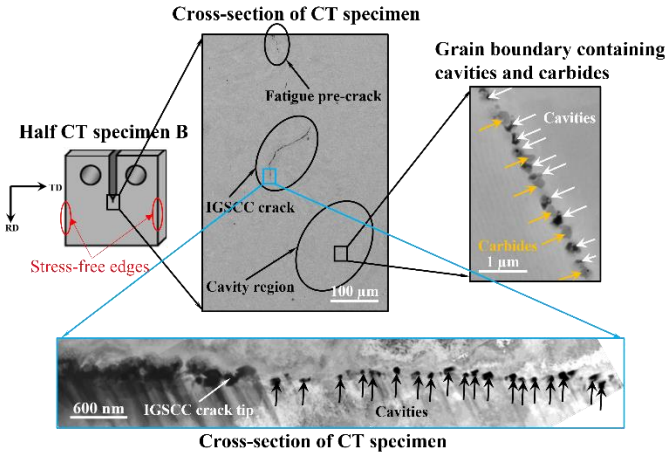

(b)

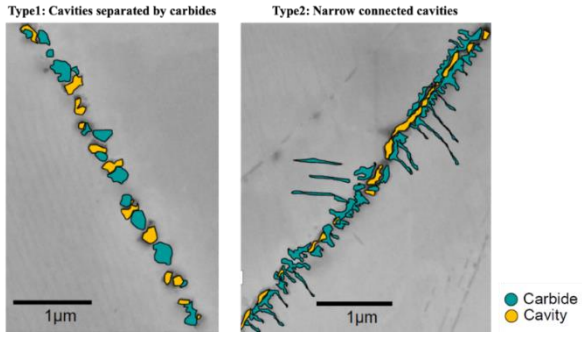

(c)

Fig. 2. Characterization of the two halves of the CT specimen to investigate the intergranular cavities around the IGSCC initiation crack. (a) Fracture surface analysis on the half CT specimen (A) showing the cavity-like morphology ahead of the IGSCC crack. (b) SEM and TEM images from the cross-section of the half CT sample (B) showing the existence of cavities near the initiation crack. (c) Two typical types of intergranular cavities.

To further analyze the morphology and distribution of the intergranular cavities in more detail, TEM analysis was conducted. Fig. 3a shows the morphology around an IGSCC crack tip. Intergranular cavities are observed ahead of the crack tip. The size of the cavities is not uniform (460 ± 170 nm). After the autoclave exposure, the IGSCC crack flanks have become oxidized, despite this material having been shown to exhibit excellent corrosion resistance [8,10]. Although the crack opening has become filled with oxides, intergranular cavities can still be observed (Fig. 3a). Fig. 3b shows a typical GB ~400 μm from the crack displaying intergranular cavities. The cavity sizes are also not uniform (~ 160 ± 110) nm. Near the edge (Fig. 2b) of the CT specimen (Fig. 3c) the sample is expected to have been nearly free of applied stress from IGSCC testing. Although no nanocavities are observed under SEM, they are observed under TEM due to the higher resolution. The size of these nanocavities is measured to be 90 ± 50 nm (Fig. 3c). Some of these cavities might be a result of the carbide fracture observed after cold-working the sample. A CSLB (Σ17) ~50 μm from the crack was also examined, as shown in Fig. 3d. Intergranular carbides are observed at this GB, although of smaller size (~20 nm vs. ~300 nm), but no cavities are found.

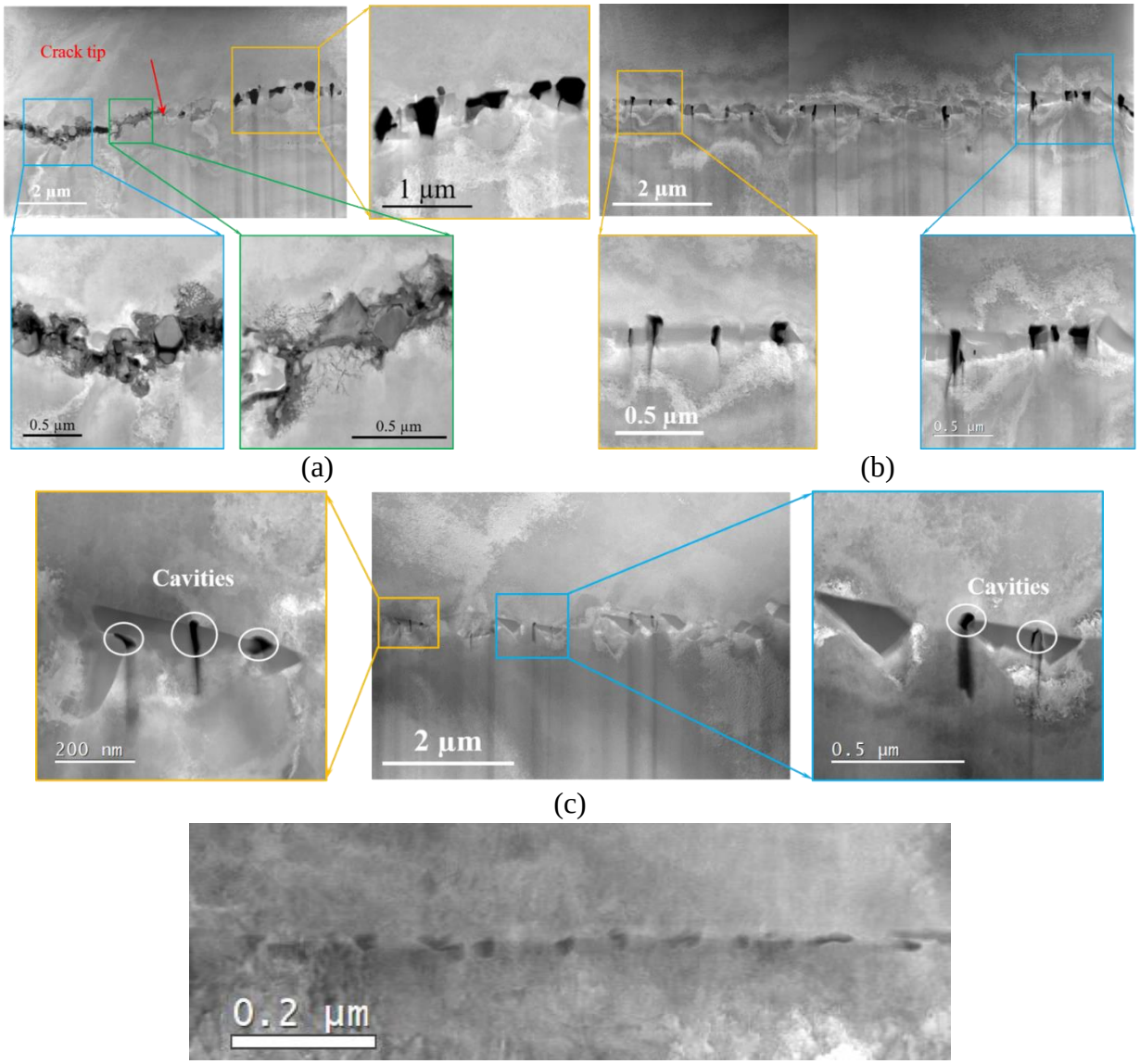

Fig. 3. HAADF images for regions taken from the cross section (half B) showing the morphology of the GBs in different regions. (a) A HAGB just ahead of the crack tip. (b) A HAGB around 400 µm from the initiation crack. (c) A HAGB at the edge of the CT specimen. (d) A CSLB (∑17) around 50 µm from the initiation crack. Note: FIB preferential milling has occurred under the cavities (darker vertical feature). This is an artifact from sample preparation.

The chemical composition of the GBs examined in Fig. 3 was analyzed by EELS. The GBs in Figs. 4a-d are correlated with those in Figs. 3a-d. It can be seen that the carbides primarily contain Cr in accordance with Fig. 1. Although the intergranular carbides in the CSLB (Σ17) are much smaller, the chemical composition distribution around this GB is generally similar to that observed in Figs. 4a-c. The only difference is the concentration of Fe across the GB is not constant, and a composition gradient also exists (Fig. 4d). The chemical composition gradients around the GBs are expected to be due to the prior thermal treatment and carbide precipitation.

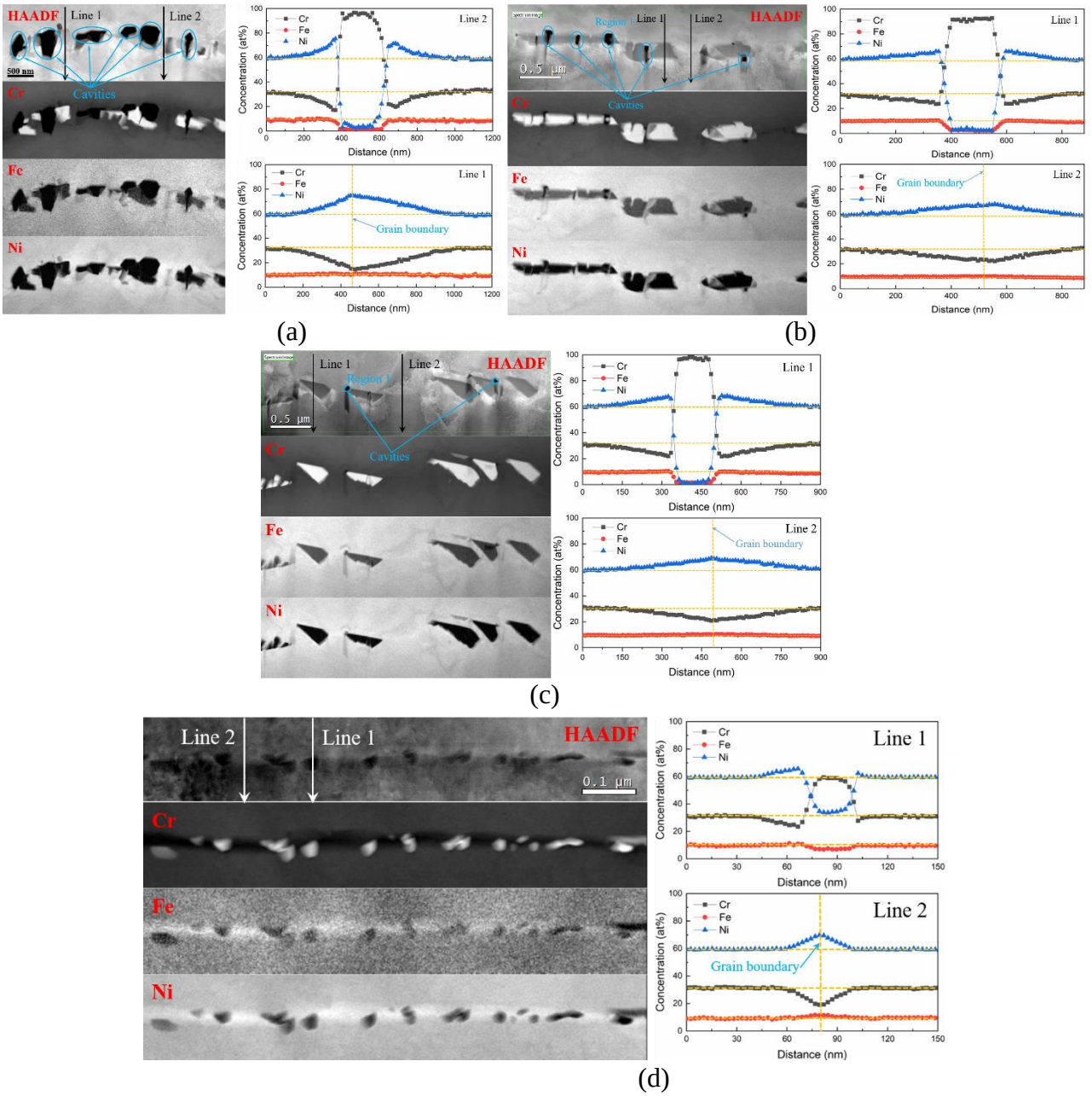

Fig. 4. EELS chemical composition maps and line-scans taken from the cross section (half A) showing the chemical composition around the GBs at different regions. (a) A HAGB just ahead of the crack tip. (b) A HAGB around 400 µm from the initiation crack. (c) A HAGB at the edge of the CT specimen. (d) A CSLB (∑17) around 50 µm from the initiation crack.

Fig. 5a shows the region around an IGSCC crack tip. The HAADF image is used to follow the open crack into the oxidized region and a tentative location for the crack tip is suggested. The 3-dimensional (3D) nature of the cracking makes its accurate location challenging. To analyse the chemical composition, EELS mapping was conducted. As shown in Fig. 5b, the intergranular carbides ahead of the crack tip are clearly visible while the intergranular carbides in the crack opening or flanks have started oxidizing or are completely dissolved, leaving behind Cr-rich oxides on the regions where were occupied by the intergranular carbides (Map 1 in Fig. 5a). The positions of the intergranular carbides are highlighted by the blue dashed circles. Intergranular cavities are also observed both ahead and behind the crack tip, which are marked by the yellow dashed circles. The interior of the cavity immediately after the crack tip (cavity 1 in Fig. 5b) is almost free of oxides although its inner surfaces

appear to be covered by a very thin Cr-rich oxide (~10 nm). Since oxides are observed in the cavity ahead the crack tip (cavity 2 in Fig. 5b), it is suggested that the oxidation does not terminate at the crack tip but advances further along some fast-diffusion channels, reaching the cavities ahead. While these cavities appear to be located ahead of the crack tip, the 3D nature of the crack means we cannot completely rule out the possibility that the cavities and the crack are connected in 3D. This issue will be further discussed later. Fig. 5c shows the morphology and chemical composition of a part of the crack which is further behind the crack tip with higher magnification (Map 2 in Fig. 5a). Since the examined region in Map 2 is further behind the crack tip, this part of crack has suffered a longer exposure to the environment than that in Map 1 and hence shows much greater oxidation. The Cr-map in Fig. 5c suggests that two cavities may have existed in this part of crack since the inner wall is covered by a thin Cr-rich oxide, which is very similar to the cavities observed in Fig. 5b. Further exposure leads to the precipitation and/or deposition of oxides in the cavities. The chemical composition maps show that the oxides in the cavities, once fully exposed to the environment, are Ni- and Fe-rich spinel. In Fig. 5d, the region in Map 3 is shown in detail. This region is beyond the intergranular oxides around the crack tip shown in Map 1. It contains two big cavities (>200 nm in diameter) and a small one ~100 nm in diameter that seems fully embedded in the matrix. All of them are in direct contact with a carbide. There are a few relevant observations in this region. The first one is that the surface of the cavities show signs of oxidation and the second one is the potential presence of oxidized dislocations emanating from the left-hand side cavity (arrowed in O map).

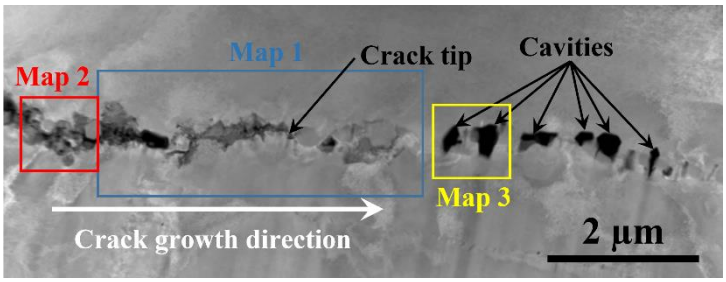

(a)

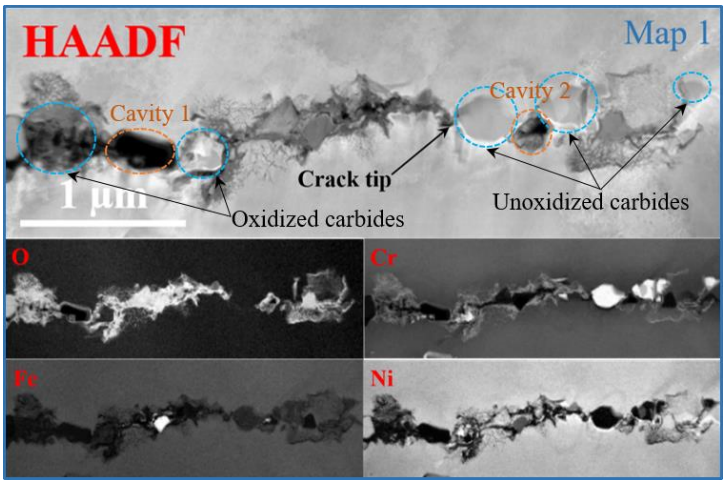

(b)

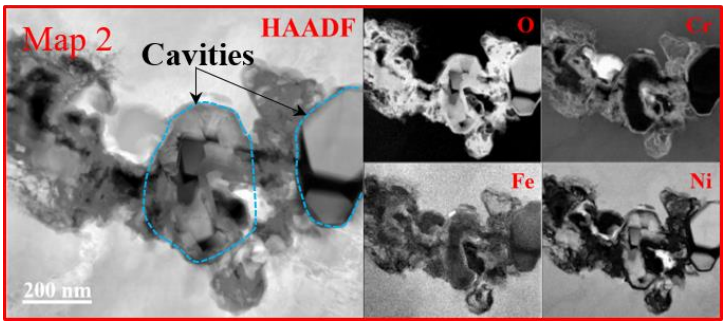

(c)

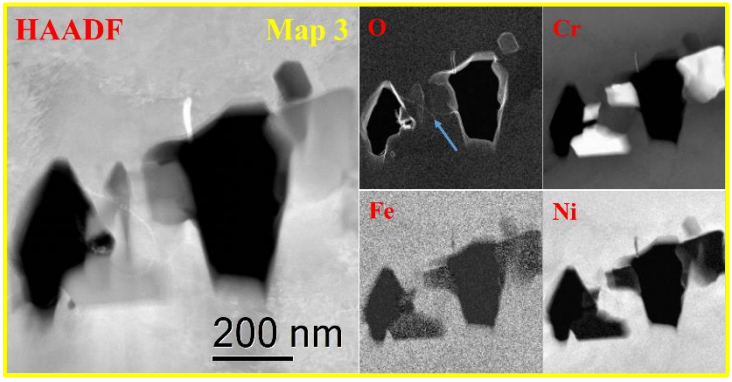

(d)

Fig. 5. Higher resolution characterization of the crack for the cross section (half A) showing the morphology and chemical composition around the initiation crack tip. (a) HAADF image. (b) HAADF image and EELS maps showing the oxidation has advanced into the region ahead of the crack tip. (c) HAADF image and EELS maps showing the existence of cavities in the wake of initiation crack. (d) HAADF image and EELS maps showing oxidation on the cavity walls and what could be oxidized dislocations emanating from the left cavity.

Following the analyses of the morphology and chemical composition of the four typical GBs in Figs. 3 and 4, the corresponding crystallographic information of the four GBs is analysed by on-axis TKD in Figs. 6a-d. The pattern quality map shows the index rate of each pixel, and a brighter tone indicates a better index rate. Since the cavities cannot be indexed, they appear black. The positions of the cavities are pointed out by the black arrows (Figs. 6a and b). Due to the small size of the cavities at the GB far away from the IGSCC crack (Fig. 4c), they are not observable under TKD analysis. The IPFZ map is used to examine the orientation between the adjacent two grains. The results show that the MO angles of the GBs in Figs. 6a-d are 34º, 48º, 37º and 50º, respectively. The MO map qualitatively indicates the extent of plastic deformation in the material. Regions of higher MO value appear “hotter” than regions of low MO value. The results show that the matrix surrounding the intergranular carbides is preferentially deformed. Some preferential deformation can still be observed in the CSLB (Σ17) even though the intergranular carbides in this GB are very small (Fig. 6d).

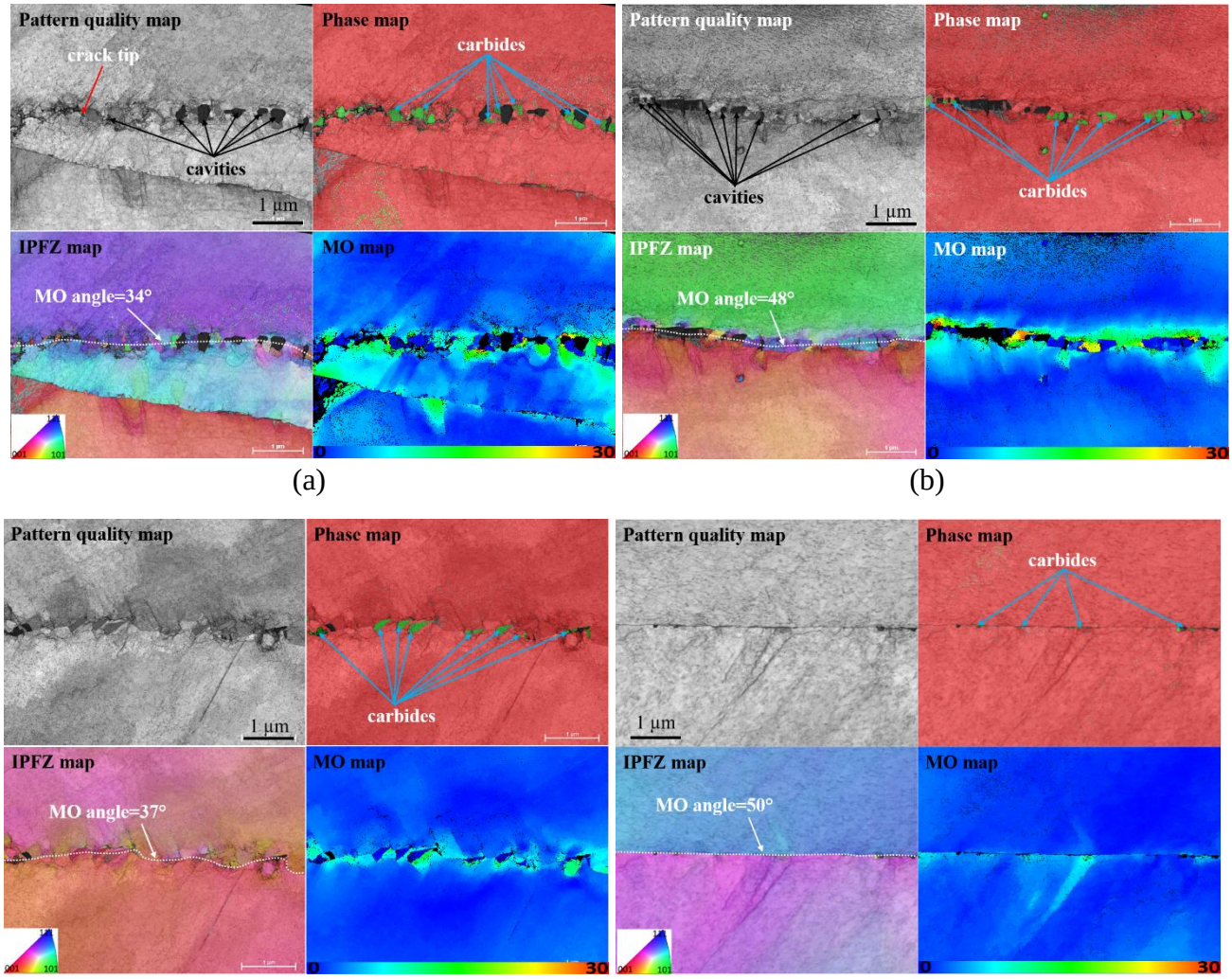

Fig. 6. On-axis TKD analysis showing the crystallographic information of the GBs at different regions. (a) A HAGB just ahead of the crack tip. (b) A HAGB around 400 µm from the initiation crack. (c) A HAGB at the edge of the CT specimen. (d) A CSLB (∑17) around 50 µm from the initiation crack. The phase map shows the different phases with carbide represented green and metal matrix in red. In the MO map the colour temperature scale ranges from blue (low) to red (high).

To quantitatively examine the extent of preferential deformation around the GBs, the geometrically necessary dislocation (GND) density was calculated from the TKD data. The local orientations as determined from TKD in a regular grid of points were used to calculate orientation differences between neighbouring points and then in turn converted to a lattice curvature estimate. This method is based on the method suggested by Wilkinson et al. [29] and Pantleon [30] and built on the local dislocation density tensor introduced by Nye [31]. More details about its application to IGSCC can be found in [32]. Given the high level of deformation caused by the prior cold-work and the associated challenges choosing a suitable reference within a grain, the GND calculations in this work are not based on high-resolution cross-correlation but on a Hough-based indexing routine instead [33]. As shown in Fig. 7, the GND values around the intergranular carbides are about 1 to 2 orders of magnitude greater than that of the other regions, suggesting the enhanced deformation around the intergranular carbides. Further observation shows that the GBs ahead of the IGSCC crack tip and adjacent to the IGSCC crack appear to have suffered greater extent of deformation than the GB far away from the IGSCC crack (Figs. 7a and b vs. Fig. 7c). The greater extent of deformation is supposed to be caused by the applied load

during the IGSCC testing. Although the CSLB (Σ17) is close to the IGSCC crack, the GND value around it is even smaller than that of the GB which is far away from the IGSCC crack. This is likely be caused by the more favourable slip transfer between the two grains and the smaller size of intergranular carbides leading to smaller preferential deformation during the prior CW [5,13].

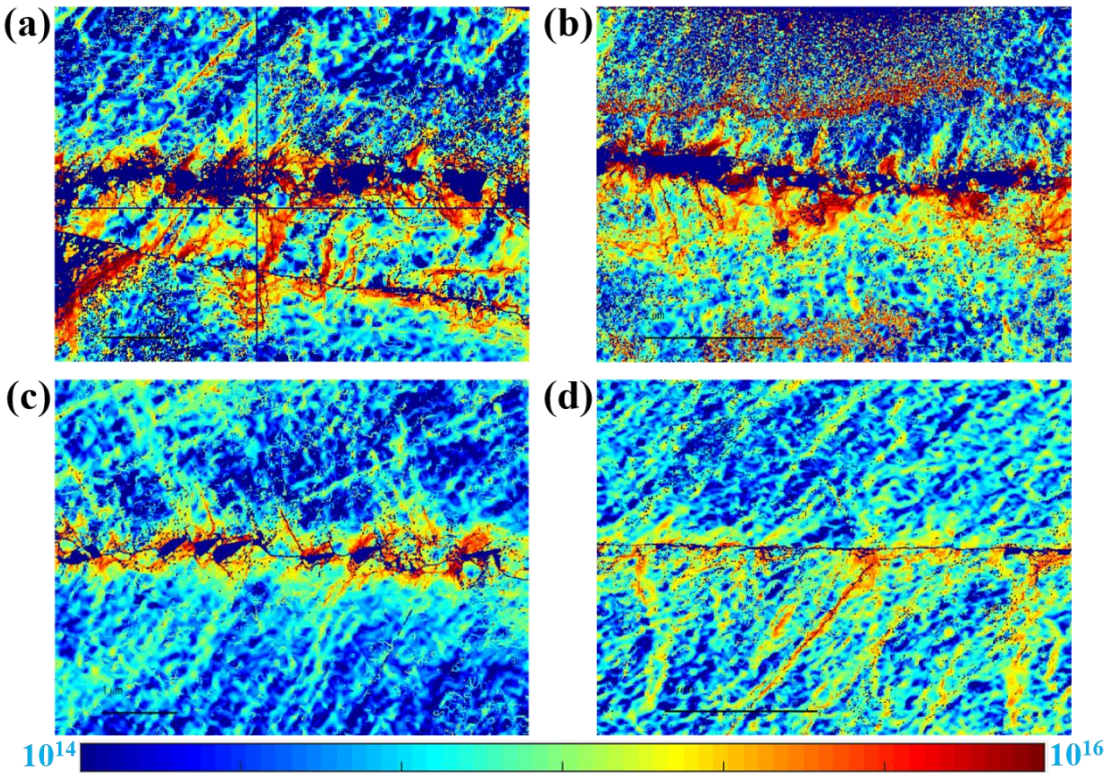

Fig. 7. Quantification of the GND values (m^{-2}) around the GBs at different regions. (a) A HAGB just ahead of the crack tip. (b) A HAGB around 400 μm from the initiation crack. (c) A HAGB at the edge of the CT specimen. (d) A CSLB (∑17) around 50 μm from the initiation crack.

3.3 Micro-mechanical testing of GBs

Although intergranular cavities are observed near the IGSCC cracks, their effect on IGSCC crack growth remains unclear. Consequently, micro-mechanical testing was conducted on the GBs containing different content of cavities to study their mechanical responses under stress, simulating that experienced during IGSCC testing. The insights obtained from this approach may help to clarify the role of intergranular cavities on IGSCC crack growth.

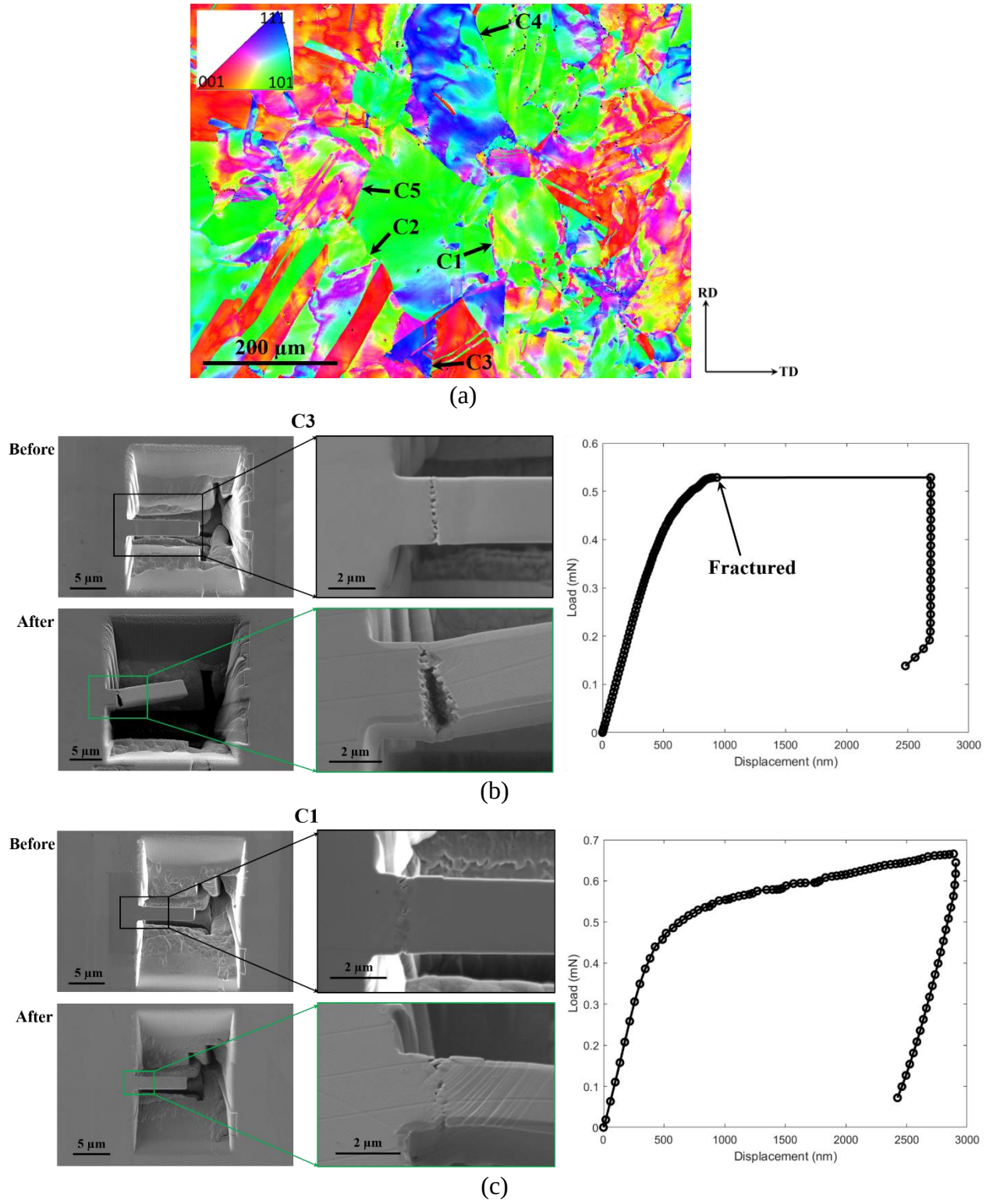

Fig. 8. Micro-mechanical testing on the five HAGBs with different intergranular carbide coverage. (a) IPFZ image with orientation legend showing the positions of the five HAGBs. (b) Morphology of GB C3 before and after the testing and related load–displacement curve. (c) Morphology of GB C1 before and after the testing and related load–displacement curve.

Of the 40 GBs that were examined and found to have cavities in the region near the crack, three GBs having different levels of cavity coverage were selected for testing, alongside two reference GBs having no cavities. These five GBs were all HAGBs and their original locations in the sample are

indicated in Fig. 8a. The MO angles, cavity and carbide coverages, Young's moduli and yield stresses of these GBs are summarized in Table 1. After the micro-mechanical testing on these cantilevers, only the GB (C3) with ~40% cavity coverage (% of GB plane covered by cavities) fractured. The morphology of this GB before and after the testing and related load–displacement curve is shown in Fig. 8b. The other GBs, having lower levels of cavity coverage (or no cavities at all), did not fracture, and only plastic deformation occurred. Fig. 8c shows the morphology of GB C1 before and after the testing, alongside the load–displacement curve. Table 1 shows an overview of the results arising from the micro-mechanical tests. The range of Young's moduli, E, for the cantilevers tested covers approximately 190-361 GPa, which is calculated using simple beam theory.

Table 1. Summary of the MO angles, cavity coverages, carbide coverages, Young's modulus, and yield stress measured from five different HAGBs.

Cantilevers	MO angle	Cavity coverage (%)	Carbide coverage	Fracture	Young's modulus (GPa)	Yield strength (GPa)
C1	37º	10	49	No	260	3.4
C2	51º	16	52	No	164	2.4
C3	48º	40	39	Yes	169	3.6
C4	54º	0	48	No	361	5.0
C5	44º	0	68	No	190	2.9

To quantify the required stress to break the GB having the higher density of cavities, finite element analysis was carried out to model the fracture in the cantilever C3 (Fig. 8b). The intergranular carbide and cavity coverages (% of the GB area) of this GB are measured to be ~39% and ~40%, respectively. The average radius of the carbides and cavities is comparable at 100 nm. A cross-section of the simulated cantilever C3 prior to fracture is presented in Fig. 9a. This shows that the cavities seem to concentrate the applied stress and prematurely initiate local boundary failure. As shown Fig. 9c, the simulated load–displacement curve (in yellow) of GB C3 fits the experimental measured load–displacement curve (in black) well. Through the simulation, it is found that the GB C3 requires 1.7 GPa to fracture. Since the other four GBs did not fracture during the micro-mechanical testing, the required stresses to break these GBs could not be obtained. The mechanical behaviour of one of the reference GBs (GB C5) during the micro-mechanical testing is simulated. There were no cavities in the GB C5 and the intergranular carbide coverage was ~68%. The average carbide radius of this GB is ~350 nm. The simulated load–displacement curve (in green) of GB C5 fits the experimental measured load–displacement curve (in black) well. Fig. 9b shows a cross-section of the simulated cantilever C5 at the end of the micro-mechanical testing. It is seen that the matrix surrounding the GB has been significantly deformed, which corresponds well with the experimental observations (Fig. 8c).

It is thought that the fracture of the GB C3 is directly linked to the high-density of cavities along the boundary plane. The fact that the GB C3 is not predicted to fracture when the intergranular cavities are removed (blue line in Fig. 9c) confirms the important role of the cavities in this case (twice that of the other samples). There may be other factors that could influence the mechanical properties and cause the GBs to fail, including the GB character and oxidation. Since the examined 5 GBs are all HAGBs, the potential effects caused by the GB character in this testing is assumed to be small. As to the potential effects caused by the oxidation, the prior SEM-EDX analysis on these five GBs (not shown) showed that none of them has been oxidized, which was expected since they were sufficiently distant from the SCC crack. Hence, any effects caused by GB oxidation can also be discounted.

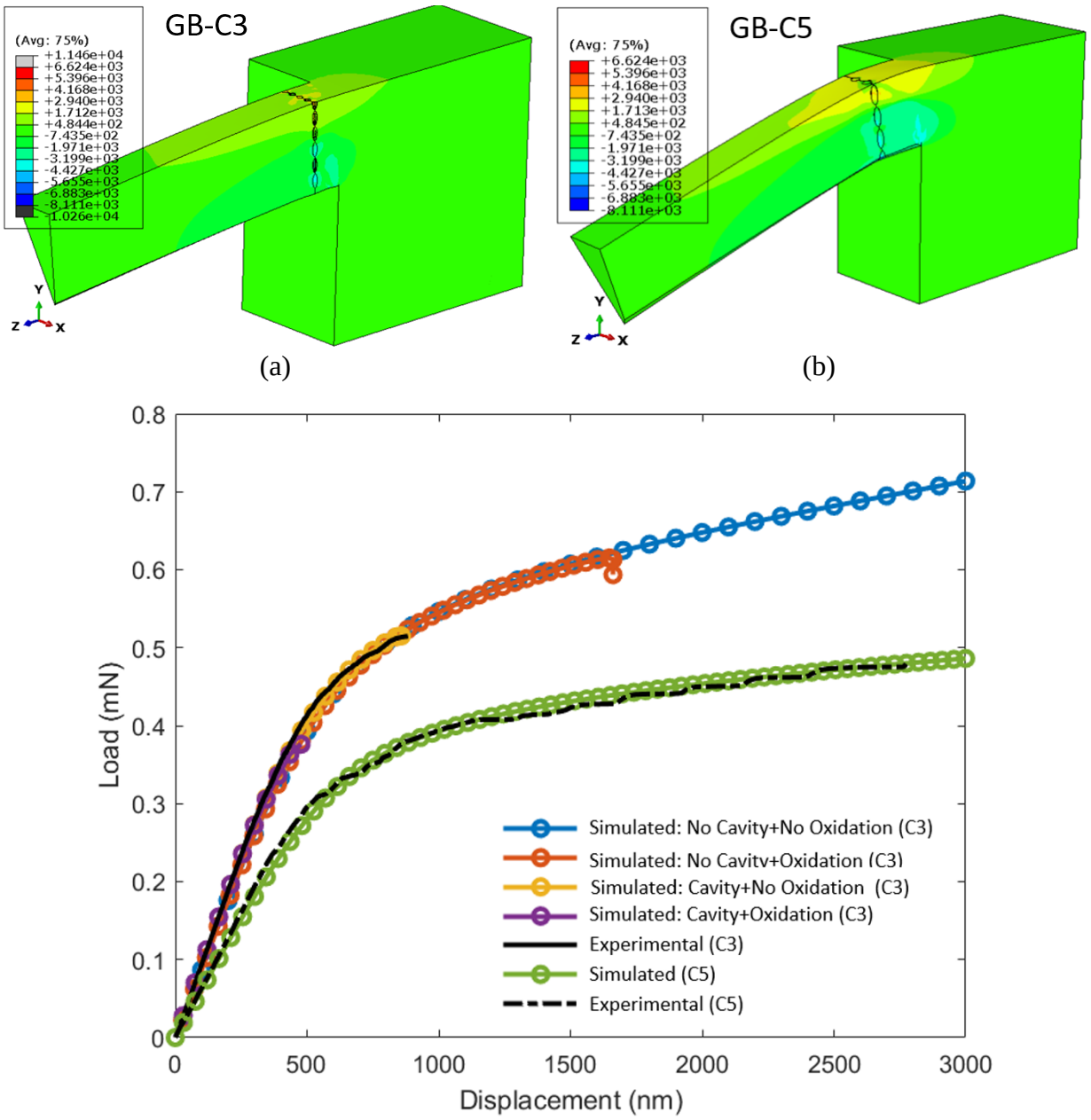

Fig. 9. Finite element analysis of the fracture and plastic deformation of the cantilevers during the micro-mechanical testing. (a) A cross-section of the simulated cantilever C3 prior to fracture. (b) A cross-section of the simulated cantilever C5 at the end of the micro-mechanical testing. (c) Experimental measured and simulated load–displacement curves of cantilevers C3 and C5.

However, the situation might be different in the region right ahead of the crack tip. Bearing in mind the uncertainties related to the crack tip exact location, Fig. 5 suggests that the oxidation may have advanced into the region ahead of the crack tip. If this is the case, the GB may have been oxidized before the IGSCC advancement and, therefore, oxidation could have also contributed to the weakening of the GB. This is also supported by the presence of oxides around the cavities ahead of the crack tip, as shown in Fig. 5d. To better understand how oxidation could have affected the GB strength, an oxidized version of GB C3 was also simulated based on the results presented by Dohr et al. [28], where the authors simulated cantilevers that contained oxidised grain boundaries and estimated the maximum stress required to fracture oxidised GBs. We have taken this value and used it as $\sigma_{ij}{}^{\max}$ in our

simulations. This value of $\sigma_{ij}{}^{\max}$ was applied to the model of cantilever GB C3, so the boundary is decorated with 39% intergranular carbides and 40% intergranular cavities. The entire grain boundary, carbide interfaces and cavities were assumed to be fully oxidised. GBs containing intergranular oxidation and cavities resulted in fracture stress falling to 1.25 GPa (purple line in Fig. 9c). This value is smaller than the GB C3 without oxidation (1.7 GPa), suggesting that the oxidation can further weaken the bonding strength of the GBs with cavities. When the 40% intergranular cavities are removed from the oxidized GB C3 (representing the simulated case of GB C3, purple line in Fig. 9c), the simulation shows that the fully-oxidized GB without cavities can be fractured under a stress of 2.0 GPa (orange line in Fig. 9c). When compared to GB oxidation, a certain amount of intergranular cavities appear to play a more critical role in weakening the GB strength (1.7 vs. 2.0 GPa).

4. Discussion

Compared with conventional "shorter" term accelerated testing under dynamic strain/stress [8,9,34-40], the mechanism controlling the "longer" term IGSCC crack growth of CW Alloy 690 under constant load is likely to be different. The present study has shown the occurrence of IGSCC crack growth and unequivocally demonstrated the formation of intergranular cavities in the region near the IGSCC crack. These cavities nucleate on the surface of intergranular Cr carbides. Some of the intergranular carbides were found to have cracked after the CW, creating an empty volume as a consequence that could resemble that of a diffusion-originated cavity. However, a clear decreasing gradient on the density and size of cavities associated with carbides was observed as one moves away from the crack tip. At distances beyond 500 μm from the crack tip, the density and size of any observed cavity was much smaller than those in the vicinity of the crack tip. These observations are consistent with the recent results obtained from the long-term IGSCC testing under constant load by the other research groups [6,7,14], while different from the results obtained from the short-term IGSCC testing under dynamic strain/stress [8,9,35,37-40], in which the IGSCC is attributed to the classic theory of rupture of intergranular oxides by the dynamic stress/strain. The observation of IGSCC cracking under the constant load and high density intergranular nanocavities in front of the crack tip in this study and in literature [6,14] suggests that a fundamentally different IGSCC mechanism in CW Alloy 690 may be operating.

In the study of the IGSCC crack growth and creep crack growth of CW Alloy 690, Arioka et al. [6] found that the crack growth rate of IGSCC and creep cracking exhibited a similar temperature dependence. These authors then proposed that the mechanism of IGSCC in CW Alloy 690 might be creep damage [6], as already suggested by Was in the 90s [REFs: Was' papers from Met Trans A]. The formation of intergranular nanocavities in the present study is also very similar to the creep cavity-related intergranular cracking, which is a commonly reported materials failure in high-temperature fossil powered plants [41,42]. Originally, the formation of creep cavities was believed to be due to the coalescence of thermal equilibrium vacancies in the material. The concentration of thermal equilibrium vacancies at 0.5 T_m (T_m: material meting point) was reported to be 10^{-6}-10^{-5} [43]. It was originally believed that more than 10^{-5} vacancy concentration was required for the formation of visibly sized cavities. In other words, observable cavities could not form at temperatures below 0.5 T_m. The experimental temperature (360 ºC) used in this study is only ~0.39 T_m of Alloy 690 (T_m: 1343-1377 ºC). As a result, the observation of intergranular nanocavities at LWRs operating temperatures is not expected. Interestingly, intergranular creep cracking of 316 steel in air and vacuum at temperatures lower than 0.5 T_m was reported in the early 1980s [44]. In addition, they found that once the 316 steel was 20% cold-worked, its crack growth rate was measured to be about 10 times faster than without CW. However, no fundamental studies were conducted to explain the occurrence of creep cracking at such low temperatures. In addition, the mechanistic studies about the CW-enhanced creep cavity-

related intergranular cracking at that time were also missing. Therefore, these early observations did not attract the interest of researchers who worked on materials degradation in LWRs.

As to the formation of unexpected creep cavities, it seems unlikely that the low concentration of thermal equilibrium vacancies at 360 ºC (~0.39 T_m) would enable 100 nm sized cavities. Additional sources of non-equilibrium vacancies should exist. Considering the 10 times faster intergranular creep crack growth rate of a 20% CW 316 steel when compared to the material without CW at temperatures below 0.5 T_m [44], it is possible that the additional non-equilibrium cavities originate from the CW in the material. The early studies have experimentally observed the generation of vacancies by plastic deformation [45]. The effects of strain on CW-induced vacancy concentration (C_v) have been studied by many researchers, and the C_v can be calculated by Equation (1) [46]:

$$\boldsymbol{C_v = \eta\varepsilon^n} \quad \textbf{(1)}$$

where ε is the strain caused by the mechanical deformation, η and n are constants. The constants of η and n are 10^{-4} and 5/4 in the early deformation stage, and 10^{-2} and 2 in the later deformation stage [43]. Then C_v for 20% CW Alloy 690 can be calculated, ranging between 1.3×10^{-5} and 4×10^{-4}. It is consistent to the concentration of thermal equilibrium vacancies at 0.6 T_m to 0.7 T_m [43]. This suggests that the CW could sufficiently decrease the required temperature for the formation of creep cavities. Although the early studies indicated that the non-equilibrium vacancies would be annihilated or concentrated at a fast speed at the PWR operating temperatures [47,48], recent studies conducted by Arioka et al. [43] showed no remarkable decrease of the CW-induced non-equilibrium vacancies at 320-500 ºC in the commercial alloys. They believed that the discrepancies may be because the early-stage vacancy annihilation studies were usually conducted in pure metals at low temperatures, while the mechanism controlling the vacancy annihilation at PWR operating temperatures in the commercial alloys may be different [43]. Although the exact causes of these discrepancies are still unknown, the observation of no significant decrease of the CW-induced non-equilibrium vacancies [49] and formation of creep cavities at temperatures below 0.5 T_m indicates that in addition to the thermal equilibrium vacancies, the CW-induced non-equilibrium vacancies may be able to contribute to the formation of creep cavities.

The stress gradient has been reported to be the driving force of vacancy diffusion under an applied stress [50]. To form the intergranular nanocavities, the vacancies in the grain interior need to diffuse to the GBs. As a result, the required time for the formation of intergranular cavities depends on the diffusion rate of the vacancies from the grain interior to the GBs. The carbide-matrix interface would act as a preferential site for cavity nucleation and alloy their growth. In the study of the effects of grain size on the creep crack growth rate of a nuclear grade Alloy 800, Arioka et al. [51] found that the crack growth rate of the fine grain material was about 10-times faster than the large grain material. The increased crack growth rate in the fine grain material was believed to be due to the relatively shorter diffusion distance decreasing the required time for the vacancy diffusion from the grain interior to the GB compared with that in the large grain material. The TKD analysis conducted in the present study shows significant preferential deformation around the intergranular carbides, while the preferential deformation in the GBs with no carbides or very small carbides is small. The preferential deformation will increase the concentration of non-equilibrium vacancies in the matrix near the GBs, which could also decrease the required time for the overall vacancy diffusion to the GBs. As a result, intergranular carbides, despite their widely reported beneficial effects on the IGSCC of Alloy 600 [13,52], could indirectly accelerate the formation of cavities in Alloy 690, contributing to the weakening of the GBs. Similar results were also reported by Kuang et al. [40] and Yonezawa et al. [53].

Our detailed high-resolution characterization reveals the formation of a high-density of intergranular nanocavities ahead of the crack tip and in the wake of the crack. This direct evidence shows that the intergranular nanocavities form before the crack propagates and, as suggested by the micromechanical testing results reported here, they are sufficient on their own to embrittle the grain boundary and allow its fracture. The micro-mechanical testing and related simulation have quantified this weakening effect. However, in a recent study of IGSCC crack growth of 20% CW Alloy 690, it was found that the crack growth rate measured in the PWR water was about 10 times faster than that measured in air, where the potential role of oxidation could be eliminated [6]. This suggests the existence of additional mechanisms in the fracture of CW Alloy 690 under simulated PWR conditions, in addition to the cavities-induced GB weakening. The selective oxidation of Cr, together with the outward diffusion of Fe ions, would also increase the local vacancy density. The observation of oxidation around the cavities ahead of the crack tip in the present study and in literature [6, 14] suggests that the high density of nanocavities ahead of the crack tip may act as pathways once interconnected for fast inward diffusion of oxidants (oxygen and/or water), resulting in oxidation in these interconnected cavities prior to the crack advancement. The higher density of dislocations observed around the carbides and cavities could act as the fast-diffusion pathways, interconnecting the nanocavities. Once the pathways formed by the interconnected cavities are contacted by any part of the open crack, a fast diffusion of oxidants can be expected, results in prior oxidation in the region ahead of the crack advancement. The decrease of GB strength after oxidation has been confirmed via micro-mechanical testing and simulation by the author's group [34,54] and the other group [55]. Although the oxidation in the GBs within nanocavities has been observed in this study, the size of the region is too small to prepare micro-cantilevers. Hence a direct measurement on the mechanical strength of the oxidized GBs within cavities was not possible. However, with the method developed for the simulation of the fracture of the oxidized GBs [34], the strength of the oxidized GBs within cavities can be simulated. The results show that the oxidation may further weaken the strength of the GBs within cavities. Consequently, not only the creep cavities but also the oxidation in the PWR primary water environment could have contributed to the crack propagation of the CW Alloy 690. The cracking of the CW Alloy 690 in the present study should be treated as a process of IGSCC instead of pure creep damage.

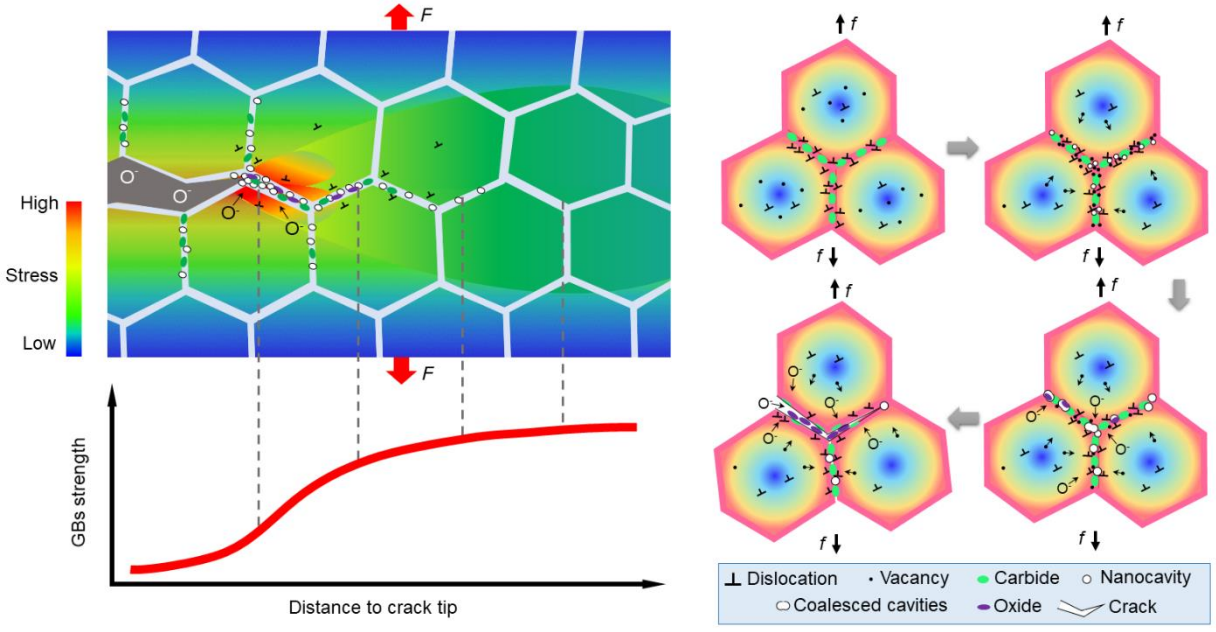

Fig. 10. Schematic images showing the intergranular nanocavities and oxidation-induced IGSCC in a CW Alloy 690.

With the results obtained in the present study and in literature [6, 7, 14, 43, 56-58], a new mechanism can be proposed to explain the long-term IGSCC of the CW Alloy 690 under a constant load in the PWR primary water, which is schematically shown in Fig. 10. In our proposed model, when a CW Alloy 690 is exposed to the PWR primary water and temperature at constant load, creep would facilitate the thermal equilibrium vacancies and non-equilibrium vacancies will diffuse to the GBs under the local stress gradient, and then coalesce to form intergranular cavities. The percentage coverage of the intergranular cavities will increase with the exposure time, resulting in the decrease of the GB strength. This, on its own, would make the alloy susceptible from cracking, although higher local stresses would be needed without the contribution of intergranular oxidation. When the coverage of the intergranular cavities reaches a critical point, aided by interconnecting dislocations, they may facilitate the inward diffusion of oxidants and the oxidation of the GBs prior to crack advancement, which will further weaken the GB strength. Once the GB strength decreases to a value that is smaller than the local stress, IGSCC crack growth occurs.

5. Conclusions

Although the observation of unexpected intergranular nanocavities in the CW Alloy 690 under constant load has been reported recently [6,7,14], a fundamental understanding of their formation and their contribution to operating mechanisms was lacking. Our work confirms the formation of intergranular nanocavities after a long-term constant load testing. The observation of nanocavities ahead of the crack tip and in the wake of the crack indicates that they form before crack advancement and then the crack advances by breaking the weakened boundary once a minimum stress is reached. The micro-mechanical testing on the GBs within high-density nanocavities and related simulation has allowed the quantification of these minimum stresses, as well as demonstrated the further weakening effect of local oxidation. It is proposed that CW Alloy 690 is not immune to long-term IGSCC and the IGSCC crack growth is believed to be the result of coupling effects of intergranular creep cavities and oxidation along these cavities once interconnected.

Acknowledgment

The authors from the University of Oxford would like to thank the EPSRC (EP/K040375/1, EP/N010868/1 and EP/R009392/1) grants for funding this research. INSS is acknowledged for providing the samples used in this study. Dr. Peter Andresen is also acknowledged for useful discussion.

6. References

[1] P.L. Andresen. Emerging issues and fundamental processes in environmental cracking in hot water. Corrosion, 64(2008) 439-464.

[2] L.E. Thomas, S.M. Bruemmer. High-resolution characterization of intergranular attack and stress corrosion cracking of Alloy 600 in high-temperature primary water. Corrosion, 56(2000) 572-587.

[3] K. Arioka, T. Yamada, T. Miyamoto, M. Aoki. Intergranular stress corrosion cracking growth behavior of Ni-Cr-Fe alloys in pressurized water reactor primary water. Corrosion, 70(2014) 695-707.

[4] G. Bertali, F. Scenini, M.G. Burke. The effect of residual stress on the preferential intergranular oxidation of alloy 600. Corrosion Science, 111(2016) 494-507.

[5] Z. Shen, M. Meisnar, K. Arioka, S. Lozano-Perez. Mechanistic understanding of the temperature dependence of crack growth rate in alloy 600 and 316 stainless steel through high-resolution characterization. Acta Materialia, 165(2019) 73-86.

[6] K. Arioka, R.W. Staehle, T. Yamada, T. Miyamoto, T. Terachi. Degradation of alloy 690 after relatively short times. Corrosion, 72(2016) 1252-1268.

[7] Z. Zhai, M. Toloczko, K. Kruska, S. Bruemmer. Precursor evolution and stress corrosion cracking initiation of cold-worked alloy 690 in simulated pressurized water reactor primary water. Corrosion, 73(2017) 1224-1236.

[8] W. Kuang, M. Song, G.S. Was. Insights into the stress corrosion cracking of solution annealed alloy 690 in simulated pressurized water reactor primary water under dynamic straining. Acta Materialia, 151(2018) 321-333.

[9] T. Moss, W. Kuang, G.S. Was. Stress corrosion crack initiation in Alloy 690 in high temperature water. Current Opinion in Solid State and Materials Science, 22(2018) 16-25.

[10] W. Kuang, X. Wu, E.H. Han, J. Rao. The mechanism of oxide film formation on Alloy 690 in oxygenated high temperature water. Corrosion science, 53(2011) 3853-3860.

[11] P.L. Andresen, M.M. Morra, K. Ahluwalia, "Effect of Deformation Temperature, Orientation and Carbide on SCC of Alloy 690", Proceedings of the 16th International Conference on Environmental Degradation of Materials in Nuclear Power Systems-Water Reactors (Houston, TX: NACE, 2013).

[12] S.M. Bruemmer, M.J. Olszta, M.B. Toloczko, L.E. Thomas. Linking grain boundary microstructure to stress corrosion cracking of cold-rolled alloy 690 in pressurized water reactor primary water. Corrosion, 69(2013), pp.953-963.

[13] Z. Shen, J. Dohr, S. Lozano-Perez. The effects of intergranular carbides on the grain boundary oxidation and cracking in a cold-worked Alloy 600. Corrosion Science, 155(2019) 209-216.

[14] K. Kruska, Z. Zhai, S.M. Bruemmer. Characterization of SCC Initiation Precursors in Cold-Worked Alloy 690. Paper presented at the CORROSION 2017, New Orleans, Louisiana, USA, March 2017.

[15] L. Luo, M. Su, P. Yan, L. Zou, D.K. Schreiber, D.R. Baer, Z. Zhu, G. Zhou, Y. Wang, S.M. Bruemmer, Z. Xu. Atomic origins of water-vapour-promoted alloy oxidation. Nature materials, 17(2018) 514-518.

[16] D.G. Xie, Z.J. Wang, J. Sun, J. Li, E. Ma, Z.W. Shan. In situ study of the initiation of hydrogen bubbles at the aluminium metal/oxide interface. Nature materials, 14(2015) 899-903.

[17] A. King, G. Johnson, D. Engelberg, W. Ludwig, J. Marrow. Observations of intergranular stress corrosion cracking in a grain-mapped polycrystal. Science, 321(2008) 382-385.

[18] Z. Shen, D. Tweddle, H. Yu, G. He, A. Varambhia, P. Karamched, F. Hofmann, A.J. Wilkinson, M.P. Moody, L. Zhang, S. Lozano-Perez. Microstructural understanding of the oxidation of an austenitic stainless steel in high-temperature steam through advanced characterization. Acta Materialia, 194(2020) 321-336.

[19] Z. Shen, K. Chen, H. Yu, B. Jenkins, Y. Ren, N. Saravanan, G. He, X. Luo, P. Bagot, M.P. Moody, L. Zhang. New insights into the oxidation mechanisms of a ferritic-martensitic steel in high-temperature steam. Acta Materialia, 194(2020) 522-539.

[20] J. Liu, S. Lozano-Perez, A.J. Wilkinson, C.R. Grovenor. On the depth resolution of transmission Kikuchi diffraction (TKD) analysis. Ultramicroscopy, 205(2019) 5-12.

[21] D.E.J. Armstrong, A.J. Wilkinson, S.G. Roberts. Micro-mechanical measurements of fracture toughness of bismuth embrittled copper grain boundaries. Philosophical Magazine Letters, 91(2011) 394-400.

[22] F. P. E. Dunne, R. Kiwanuka, A. J. Wilkinson. Crystal plasticity analysis of micro-deformation, lattice rotation and geometrically necessary dislocation density. Proceedings of the Royal Society A: Mathematical, Physical and Engineering Sciences, 468(2012) 2509-2531.

[23] Edward Roberts, Zhao Shen, David Armstrong, Koji Arioka, Florence Carrette, Sergio Lozano-Perez, Edmund Tarleton. The effects of intergranular carbides and cavitation on the bonding strength of grain boundaries in alloy 690, submitted to “Applied Surface Science”, Under Review.

[24] R. Toda. Lattice strain development in Inconel-690 under bi-axial compression and tension (Doctoral dissertation, 2010).

[25] B. Xiao, J. Feng, C.T. Zhou, Y.H. Jiang, R. Zhou. Mechanical properties and chemical bonding characteristics of Cr7C3 type multicomponent carbides. Journal of Applied Physics, 109(2011) 023507.

[26] M.E. Kartal, R. Kiwanuka, F.P.E. Dunne. Determination of sub-surface stresses at inclusions in single crystal superalloy using HR-EBSD, crystal plasticity and inverse eigenstrain analysis. International Journal of Solids and Structures, 67(2015) 27-39.

[27] F.P.E. Dunne, D. Rugg, A. Walker. Lengthscale-dependent, elastically anisotropic, physically-based hcp crystal plasticity: application to cold-dwell fatigue in Ti alloys. International Journal of Plasticity, 23(2007) 1061-1083.

[28] J. Dohr, D.E. Armstrong, E. Tarleton, T. Couvant, S. Lozano-Perez. The influence of surface oxides on the mechanical response of oxidized grain boundaries. Thin Solid Films, 632(2017) 17-22.

[29] A. J. Wilkinson, D. Randman. Determination of elastic strain fields and geometrically necessary dislocation distributions near nanoindents using electron back scatter diffraction, Philosophical Magazine, 90(2010) 1159-1177.

[30] W. Pantleon. Resolving the geometrically necessary dislocation content by conventional electron backscattering diffraction, Scripta Materialia, 58(2008) 994-997.

[31] J.F Nye. Some geometrical relations in dislocated crystals, Acta Metallurgica, 1(1953) 153-162.

[32] N. Saravanan, P.S. Karamched, J. Liu, E. Burger, F. Scenini, S. Lozano-Perez. Using local GND density to study SCC initiation. 217(2020) 113054.

[33] P.J. Konijnenberg, S. Zaefferer, D. Raabe. Assessment of geometrically necessary dislocation levels derived by 3D EBSD. Acta Materialia, 99(2015) 402-414.

[34] W. Kuang, M. Song, X. Feng. Insight into the acceleration in oxidation kinetics ahead of stress corrosion crack of alloy 690 in simulated PWR primary water. Corrosion Science, 176(2020) 108943.

[35] K. Chen, J. Wang, Z. Shen, D. Du, X. Guo, B. Gong, J. Liu, L. Zhang. Comparison of the stress corrosion cracking growth behavior of cold worked Alloy 690 in subcritical and supercritical water. Journal of Nuclear Materials, 520(2019) 235-244.

[36] T. Yonezawa, K. Onimura, N. Sasaguri, T. Kusakabe, H. Nagano, K. Yamanaka, T. Minami, M. Inoue. Effect of heat treatment on corrosion resistance of Alloy 690, in: Proceedings of the Second International Symposium on Environmental Degradation of Materials in Nuclear Power Systems-Water Reactors, Monterey, California, 1985.

[37] W. Kuang, H. Yue, X. Feng, B. Yang, C. Guo. A novel test technique for the mechanistic study of initiation of environmentally assisted cracking on a Ni–30Cr–10Fe alloy in simulated pressurized water reactor primary water. Scripta Materialia, 189(2020) 122-128.

[38] J.B. Ferguson, H.F. Lopez. Oxidation products of Inconel alloys 600 and 690 in pressurized water reactor environments and their role in intergranular stress corrosion cracking. Metallurgical and Materials Transactions A, 37(2006) 2471-2479.

[39] T. Moss, G.S. Was. Accelerated stress corrosion crack initiation of alloys 600 and 690 in hydrogenated supercritical water. Metallurgical and Materials Transactions A, 48(2017) 1613-1628.

[40] W. Kuang, G.S. Was. The effects of grain boundary carbide density and strain rate on the stress corrosion cracking behavior of cold rolled Alloy 690. Corrosion Science, 97(2015) 107-114.

[41] N.D. Evans, P.J. Maziasz, R.W. Swindeman, G.D. Smith. Microstructure and phase stability in INCONEL alloy 740 during creep. Scripta Materialia, 51(2004) 503-507.

[42] F. Sun, Y.F. Gu, J.B. Yan, Z.H. Zhong, M. Yuyama. Phenomenological and microstructural analysis of intermediate temperatures creep in a Ni–Fe-based alloy for advanced ultra-supercritical fossil power plants. Acta Materialia, 102(2016) 70-78.

[43] K. Arioka. Role of Cavity Formation on Long-Term Stress Corrosion Cracking Initiation: A Review. Corrosion, 76(2020) 142-175.

[44] K. Sadananda, P. Shahinian. Effect of environment on crack growth behavior in austenitic stainless steels under creep and fatigue conditions. Metallurgical transactions A, 11(1980) 267-276.

[45] J. Molenaar, W.H. Aarts. Change of resistivity by cold working at liquid-air temperature. Nature, 166(1950) 690-690.

[46] H.G. Van Bueren. Theory of the formation of lattice defects during plastic strain. Acta Metallurgica, 3(1955) 519-524.

[47] S.J. Rothman, N.L. Peterson, J.T. Robinson. Isotope Effect for Self-Diffusion in Single Crystals of Silver. Physica Status Solidi (b), 39(1970) 635-645.

[48] Y. Iijima, K. Kimura, K. Hirano. Self-diffusion and isotope effect in α-iron. Acta Metallurgica, 36(1988) 2811-2820.

[49] K. Arioka, Y. Iijima, T. Miyamoto. Rapid nickel diffusion in cold-worked carbon steel at 320–450° C. Philosophical Magazine, 95(2015) 3577-3589.

[50] C. Herring. Deformation of Crystals by the Motion of Single Ions. J. Appl. Phys., 21(1950) 437.

[51] K. Arioka, R.W. Staehle, R.L. Tapping, T. Yamada, T. Miyamoto. Stress Corrosion Cracking Growth of Alloy 800NG in Pressurized Water Reactor Primary Water. Corrosion, 74(2018) 24-36.

[52] Z. Shen, J. Liu, K. Arioka, S. Lozano-Perez. On the role of intergranular carbides on improving the stress corrosion cracking resistance in a cold-worked alloy 600. Journal of Nuclear Materials, 514(2019) 50-55.

[53] T. Yonezawa, A. Hashimoto, Effect of Cold Working and Long-Term Heating in Air on the Stress Corrosion Cracking Growth Rate in Commercial TT Alloy 690 Exposed to Simulated PWR Primary Water. Metall Mater Trans A 52(2021) 3274–3288.

[54] H. Dugdale, D.E. Armstrong, E. Tarleton, S.G. Roberts, S. Lozano-Perez. How oxidized grain boundaries fail. Acta Materialia, 61(2013) 4707-4713.

[55] K. Fujii, T. Miura, H. Nishioka, K. Fukuya. Degradation of grain boundary strength by oxidation in alloy 600. In Proceedings of the 15th International Conference on Environmental Degradation of Materials in Nuclear Power Systems—Water Reactors (pp. 1447-1461). Springer, Cham, 2011.

[56] J. L. Hertzberg, G. S. Was. Isolation of carbon and grain boundary carbide effects on the creep and intergranular stress corrosion cracking behavior of Ni-16Cr-9Fe-xC alloys in 360 C primary water. Metallurgical and Materials Transactions A, 29(1998) 1035-1046.

[57] T. M. Angeliu, G. S. Was. Creep and intergranular cracking of Ni-Cr-Fe-C in 360 C argon. Metallurgical and Materials Transactions A, 25(1994) 1169-1183.

[58] Sung, J. K., Jones, J. W., & Was, G. S. (1992). Effect of carbon on the low-temperature creep behavior of Ni-16Cr-9Fe. Metallurgical Transactions A, 23(3), 1033-1037.